Advanced Steel Construction – Vol. 22 No. 2 (2026) 222–236
DOI:10.18057/IJASC.2026.22.2.8

STUDY ON BAND GAP CHARACTERISTICS OF PERIODIC GRID STRUCTURE AND SHOCK WAVE ATTENUATION IN IT

Hai-Xiang Zhao [1], Bai-Qian Sun [1], En Zhang [2], Zhi-Xing Wang [3], Li-Gang Zheng [3], Qian Yang [3], Peng-Cheng Chen [1, *] and Guo-Yun Lu [1]

[1] *College of Civil Engineering, Taiyuan University of Technology, Taiyuan 030024, Shanxi, China*
[2] *Department of Architecture and Environmental Engineering, Taiyuan University, Taiyuan 030032, Shanxi, China*
[3] *Shanxi Xiaohe Construction Industry Co., Ltd, Taiyuan 030032, Shanxi, China*
** (Corresponding author: E-mail: chenpengcheng@tyut.edu.cn)*

ABSTRACT

The unique band gap characteristics of periodic structures result in varying degrees of attenuation of elastic wave propagation across different frequency ranges. With the increasing demand for periodic grid structures, particularly long-span grids, in various sectors of industry and daily life, the issues of vibration reduction and isolation in such structures have become increasingly prominent. Inspired by the periodic properties of phononic crystals, this study conducts a mechanical analysis of grid rod elements, derives the corresponding periodic equations, and investigates their underlying periodic mechanisms. Numerical simulations confirm the existence of band gaps in steel and aluminum hybrid grid rods and examine the effects of the rod's Elastic modulus, density, and inner radius on these band gap characteristics. Finally, the impact attenuation performance of the steel–aluminum hybrid grid rod is compared with that of pure steel and pure aluminum grid rods. The results show that: (1) with increasing Elastic modulus, the starting frequency, end frequency, and width of the widest band gap all increase, while the starting frequency, end frequency, and width of the 13th-order band gap first increase and then disappear; (2) with increasing density, the width of the widest band gap decreases, and the starting frequency, end frequency, and width of the 16th-order band gap all decrease until it disappears; (3) with increasing inner radius, the width of the widest band gap increases, and the starting frequency, end frequency, and width of the 19th-order band gap all increase, with low-frequency band gaps gradually emerging; and (4) compared to steel and aluminum grid rods, the steel and aluminum hybrid grid rod exhibits superior impact wave attenuation performance, with the band gap characteristics of single-rod elements playing a critical role in suppressing vibrations throughout the entire grid structure.

ARTICLE HISTORY

Received: 11 March 2025
Revised: 4 July 2025
Accepted: 18 July 2025

KEYWORDS

Periodic structures;
Grid structure;
Band gap;
Vibration reduction and isolation;
Steel structure

1. Introduction

Grid structures exhibit excellent performance under extreme loads, such as large earthquakes. Therefore, large-scale buildings employing this structural form are often designated by the state as disaster shelters, highlighting the importance of evaluating their resilience under extreme conditions[1-4]. The safety of these structures is crucial for protecting public lives and ensuring social stability. As a result, progressive collapse in large-span structures has become a significant research focus, aiming to understand their sequential failure processes and anti-collapse mechanisms under sudden extreme loads. Given the waveguide properties inherent to periodic grid structures, stress waves generated by dynamic loads or group failures propagate within the structure. Due to the dispersive properties of periodic structures[5-8], phenomena such as wave blockage or localized resonance may occur[9], potentially leading to the localized storage of energy, causing member vibration buckling, pulse buckling, or even node fractures.

According to stress wave theory, stress and strain caused by vibrations primarily propagate through structures in the form of waves[10]. Periodic structures have attracted significant attention from researchers due to their desirable vibration-damping properties, which can block the propagation of stress waves. Effectively enhancing and leveraging the periodic properties of structures to achieve vibration damping is a current research hotspot. In 1992, M.M. Sigalas theoretically demonstrated the existence of elastic wave band gaps in three-dimensional periodic lattice structures made of composite materials, wherein elastic waves with frequencies within these gaps cannot propagate[11]. This concept evolved from the Bragg scattering mechanism to the localized resonance band gap mechanism, significantly broadening the range of wavelengths corresponding to band gap frequencies. Today, periodic structures find extensive applications in defense, aerospace[12], marine[13], and other fields. Michele Brun introduced the concept of phononic band gaps in structural mechanics, using waveguide properties to address vibration problems in slender bridges and extending this application to vibration reduction in high-rise structures[14].

The inherent wave conversion and frequency band gap characteristics of periodic structures lead to the suppression of elastic wave transmission within certain frequency ranges[15-16]. This underscores how innovative design and optimization based on structural periodicity can achieve effective vibration isolation. Muhammad et al. proposed sinusoidal connecting elements in two-dimensional periodic structures and found that certain geometric parameters influence the transmission and blocking characteristics of these structures[17]. Several scholars have conducted studies on concrete metamaterials, impact mitigation, vibration resistance, and blast resistance[18-22]. Feng[23] studied a two dimensional tunable acoustic crystal based on square rods. In this structure, 1.6 mm wide steel rods are arranged in air. By introducing variations in the scattering interface through symmetry breaking, achieved by simply rotating the square rods, the scattering cross section corresponding to different geometric factors changes from positive to negative refraction. This enables control over wave propagation and achieves tunable refraction of acoustic waves. Shen et al.[24] applied phononic crystal theory to guide the design of periodic structures in seawater pipeline systems. The designed structure can regulate the propagation characteristics of vibroacoustic waves within specific frequency bands, thereby achieving vibration reduction in the pipeline system. However, limited research has been carried out on the periodic properties of large-scale grid structures, which are most similar to crystal lattice structures, from the perspective of wave propagation and dispersion. This research gap is partly due to the conventional belief among engineers that the instantaneous nature of wave propagation does not significantly affect structural collapse[25], and partly due to the requirement that periodic dimensions must be approximately half the wavelength of elastic waves to realize Bragg band gaps[26-27]. Consequently, flat grid structures are often not considered to exhibit band gap properties. In reality, the concept of localized resonance has greatly extended these wavelength conditions. Previous discussions also indicate that the condition of matching half-wavelengths to member lengths is achievable. Numerical simulations of real structures have shown that grid structures exhibit characteristics of periodic structural responses. However, due to their three-dimensional forms and the coupling of bending and axial longitudinal waves, the analysis becomes more complex, resulting in narrower band gaps that are harder to detect. An, et al.[28] fabricated a three-dimensional acoustic metamaterial featuring a truss lattice structure using additive manufacturing techniques. Employing finite element analysis and numerical simulations, they systematically investigated the band structure of the proposed lattice and identified band gaps arising from local resonance and wave mode conversion. Zuo, et al. optimized the design of periodic rigid grid structures by altering unit shapes and geometric parameters, identifying factors that influence band gap characteristics[29]. Meruane, et al. proposed a new design of sandwich panels with cellular truss cores, aimed to harness these band gaps to achieve pronounced wave suppression within specific frequency ranges[30]. Modern

materials with complex architectures show higher structural efficiency when compared to traditional materials, Quinteros, et al. designed two-dimensional truss-like cellular structures to find best frequency range of each truss element[31]. By designing the structural parameters of periodic structures effectively, vibration isolation performance can be optimized.

Applications of periodic characteristic analysis in large bridge structures[32-33] and foundations[34] have demonstrated that macro-scale periodic structures also possess inherent band gap and dispersion properties. Some literature suggests that structural collapse may be caused by failure waves propagating within large structures[35]. Therefore, studying wave propagation characteristics in grid structures is essential for predicting structural health and providing theoretical explanations for certain failure causes. Using grid structures as research targets for wave dynamics within periodic structures offers advantages not found in lattice materials. This will promote the development of periodic structure research and help explain grid structure collapse incidents, guiding anti-collapse design through waveguide properties.

2. Mechanical Modeling Analysis of grid structure rod unit

2.1. grid structure rod unit

A large-scale grid structure consists of fundamental units connected in a periodic configuration, forming a highly redundant spatial system through the systematic arrangement of multiple members joined at nodes in a defined repeating pattern. The intersecting members and nodes provide mutual support in three dimensions, while the inherent vibration isolation characteristics of periodic structures further enhance their performance. As a result, grid structures possess wider applicability compared to planar trusses, which predominantly carry unidirectional loads. An illustrative example is the double-layer grid structure with a quadrangular pyramid configuration, as shown in Fig. 1.

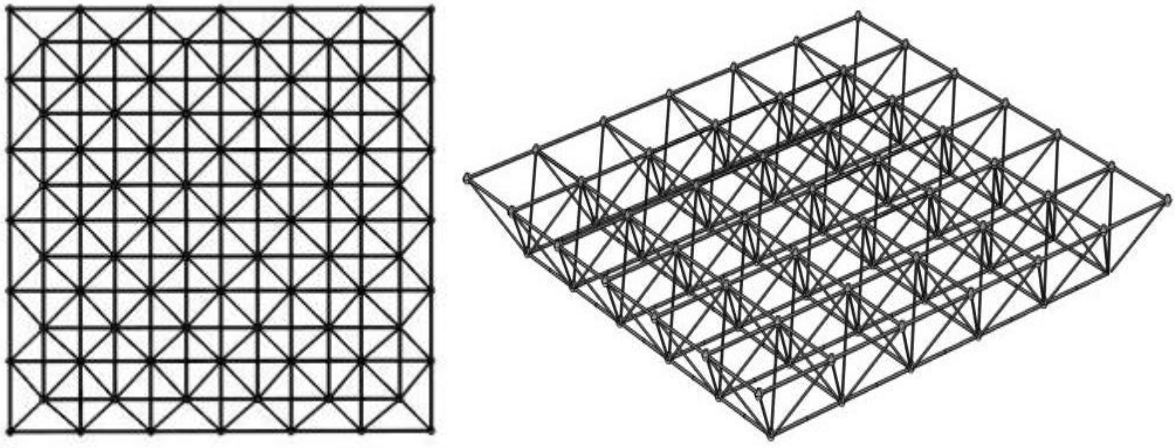

(a) Planar periodic grid structure (b)Three-dimensional diagram of periodic grid structure

Fig. 1 Periodic quadrangular pyramid grid

Grid structures are a type of periodic structure formed by the periodic arrangement of joints and members. This structure is created by repeating a minimal unit in a topological pattern, which allows for the analysis of the dynamic characteristics of grid structures to begin with a simplified dynamic analysis of the minimal unit and then extend to the entire structure. A quadrangular pyramid grid structure can be viewed as being composed of several quadrangular pyramids, as shown in Fig. 2.

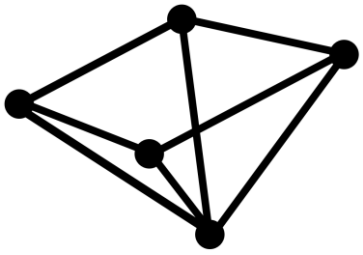

Fig. 2 Four-sided pyramid unit

Each quadrangular pyramid grid unit consists of several spherical nodes and members. When studying periodic structures, it is common practice to select the smallest periodic unit. Therefore, research into the band gap characteristics of periodic grid structures should begin with the member units, as illustrated in Fig. 3.

Fig. 3 grid structure rod unit

2.2. Periodical analysis of grid structures

When analyzing the band gap characteristics of periodic structures, it is essential to select a computational method appropriate to the specific features of the structure. The choice of method influences both the computational efficiency and the accuracy of the results. Over the years, through the research of many scholars, various methods for solving the bandgap have emerged, including the Plane Wave Expansion method (PWE)[36-38] and the Transfer Matrix method (TM)[39-41], et al. For the simplified mechanical analysis of grid structures, this section presents the transfer equation for the vibration response of member units within the grid structure. Since the grid structure exhibits periodicity, its analysis can be effectively carried out by examining the smallest repeating unit, applying appropriate boundary conditions, and solving accordingly. This section focuses on the dynamic analysis of the grid structure's member units. While members are typically idealized as axially loaded elements in conventional analyses, dynamic loading can excite a variety of vibration modes. As a result, members may display complex wave behavior beyond simple longitudinal compression and tension, including bending, torsional, and shear waves. Therefore, the member units are modeled as bending beam elements, as depicted in Fig. 4, with each unit characterized by two translational degrees of freedom and one rotational degree of freedom.

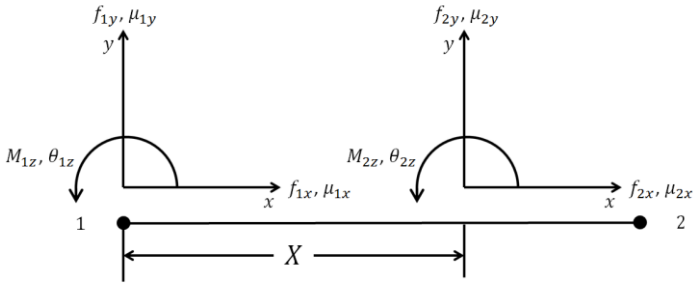

Fig. 4 Analysis model of single rod vibration

The input and output parameters of the rod cell vector in the smallest unit body of the grid structure in the local coordinate system are represented as follows:

$$S_1 = \{f_{1x}, f_{1y}, M_{1z}, u_{1x}, u_{1y}, \theta_{1z}\} \tag{1}$$

$$S_2 = \{f_{2x}, f_{2y}, M_{2z}, u_{2x}, u_{2y}, \theta_{2z}\} \tag{2}$$

Where f is the external load of the rod, M is the torque, u is the displacement value of the vibration response, θ is the angular displacement value of the torsional response, the subscripts x, y, z of each equation represent the axial, transverse and longitudinal directions of the coordinate system, respectively, and 1, 2 are the two end point marks. S_1 and S_2 represent the state vectors at the two end points.

The bending moment vibration equation is:

$$\frac{\partial f_y}{\partial x} + \frac{\partial f_x}{\partial R_m} = \rho h \ddot{u}_y \tag{3}$$

$$\frac{\partial f_x}{\partial x} + \frac{\partial f_y}{\partial R_m} = \rho h \ddot{u}_x \tag{4}$$

Where ρ for the material density, h for the equivalent height of beam section, R_m for the bending beam radius of curvature.

For the bending vibration equation, f_x, f_y, M_z can be solved using the equations from strength of materials.

According to the bending theory in mechanics of materials, for a curved beam with a radius of curvature R_m:

$$\varepsilon_x = \varepsilon_0 + y\kappa_z = \left(\frac{\partial u_x}{\partial x} - \frac{u_y}{R_m}\right) + y\kappa_z \tag{5}$$

Taking into account the effect of curvature on the elongation of any fiber within the curved beam, the resulting force is given by:

$$f_x = \int_A \sigma_x dA = E\int_{-\frac{h}{2}}^{\frac{h}{2}} \frac{\varepsilon_x + y\kappa_z}{1 + \frac{y}{R_m}} h dy = Eh\int_{-\frac{h}{2}}^{\frac{h}{2}} \frac{\varepsilon_x + y\kappa_z}{1 + \frac{y}{R_m}} dy \tag{6}$$

Since the rod is simplified as a curved beam, the axial strain distribution differs from the linear pattern observed in straight beams. Due to geometric nonlinear effects, the fiber length varies with the position Y, and therefore a correction term $1 + \frac{y}{R_m}$ is introduced.

According to shear deformation theory, the shear strain is given by:

$$\gamma_{xy} = \frac{\partial u_y}{\partial x} + \frac{u_x}{R_m} - \theta_z \tag{7}$$

Shear deformation is not merely a simple geometric slope variation; it also involves a combined effect of curvature and rotation. Therefore, the shear force can be expressed as:

$$f_y = \kappa G h \gamma_{xy} = \kappa G h \left(\frac{\partial u_y}{\partial x} + \frac{u_x}{R_m} - \theta_z\right) \tag{8}$$

The bending moment of the structure about the neutral axis z is expressed as:

$$M_z = \int_A y\sigma_x dA \tag{9}$$

Assuming a linear strain distribution and still using Eq.(5) as the axial strain, we obtain:

$$M_z = E\int_{-h/2}^{h/2} y\left(\left(\frac{\partial u_x}{\partial x} - \frac{u_y}{R_m}\right) + y\kappa_z\right) dy \tag{10}$$

The symmetric integral of the first term is zero, yielding:

$$M_z = EZ_2\left(\frac{\partial u_x}{\partial x} - \frac{u_y}{R_m} - R_m\frac{\partial \theta_z}{\partial x}\right) \tag{11}$$

According to planar bending theory, $\frac{\partial u_x}{\partial x} - \frac{u_y}{R_m} - R_m\frac{\partial \theta_z}{\partial x}$ represents the actual state of neutral bending and distortion under the applied loads.

In Eq.(6), $\varepsilon_x = \frac{\partial u_x}{\partial x} - \frac{u_y}{R_m}$, which is the longitudinal strain induced by longitudinal expansion combined with transverse bending, $\kappa_z = \frac{\partial \theta_z}{\partial x}$, which is the axial strain induced by torsion, and $Z_2 = -R_m h Z^*$, $Z^* = \frac{R_m}{h} ln\left(\frac{h}{R_m} + 1\right) - 1$, where G is the shear stiffness and κ is the shear constant. The expressions for ε_x and κ_z are substituted into Eq.(6) for simplification to obtain the following equation:

$$f_x = Eh\left(\frac{\partial u_x}{\partial x} - \frac{u_y}{R_m}\right)\int_h \frac{1}{1+\frac{y}{R_m}} dy + Eh\frac{\partial \theta_z}{\partial x}\int_h \frac{y}{1+\frac{y}{R_m}} dy \tag{12}$$

The integral term in Eq.(12) can be simplified, and the equation is as follows:

$$\int_h \frac{1}{1+\frac{y}{R_m}} dy = R_m ln\left(\frac{h}{R_m} + 1\right) = R_m h - R_m^2 ln\left(\frac{h}{R_m} + 1\right) \tag{13}$$

By substituting the simplified integral term into the original equation, the following expression is obtained:

$$f_x = EhZ_1\left(\frac{\partial u_x}{\partial x} - \frac{u_y}{R_m}\right) + EhZ_2\frac{\partial \theta_z}{\partial x} \tag{14}$$

where $Z_1 = h(1 + Z^*)$, and then by simultaneously solving Eqs.(3), (4), (6), (8), (11) and (14), we obtain the solution for the vector $S = \{f_x, f_y, M_z, u_x, u_y, \theta_z\}$, where differential matrix equation of each parameter is as follows:

$$B\frac{\partial S}{\partial x} = AS \tag{15}$$

$$A = \begin{bmatrix} 0 & \frac{1}{R_m} & 0 & -\rho h\omega^2 & 0 & 0 \\ -\frac{1}{R_m} & 0 & 0 & 0 & -\rho h\omega^2 & 0 \\ 0 & -1 & 0 & 0 & 0 & \frac{-\rho h^3\omega^2}{12} \\ \frac{1}{EhZ_1} & 0 & 0 & 0 & \frac{1}{R_m} & 0 \\ 0 & \frac{1}{\kappa Gh} & 0 & -\frac{1}{R_m} & 0 & 1 \\ 0 & 0 & -\frac{1}{EZ_2R_m} & 0 & -\frac{1}{R_m^2} & 0 \end{bmatrix} \tag{16}$$

$$B = \begin{bmatrix} 1 & 0 & 0 & 0 & 0 & 0 \\ 0 & 1 & 0 & 0 & 0 & 0 \\ 0 & 0 & 1 & 0 & 0 & 0 \\ 0 & 0 & 0 & 1 & 0 & -\frac{Z_2}{Z_1} \\ 0 & 0 & 0 & 0 & 1 & 0 \\ 0 & 0 & 0 & 0 & \frac{1}{R_m} & 1 \end{bmatrix} \tag{17}$$

where ω is the angular frequency.

The structure model is solved under harmonic excitation, and the solution to the equation is:

$$S(x) = B_0 e^{\lambda x} \tag{18}$$

Substituting Eq.(18) into the matrix equation and solving, we obtain the following expression:

$$[B^{-1}A - \lambda I]B_0 = 0 \tag{19}$$

Since the necessary and sufficient condition for a nonzero solution in matrix equations is that the determinant of the coefficient matrix must be zero, the following system of equations is obtained:

$$det[B^{-1}A - \lambda I] = 0 \tag{20}$$

Solving this matrix equation gives the characteristic root λ_i:

$$S(x) = B_0 \begin{pmatrix} e^{\lambda_1 x} & \cdots & 0 \\ \vdots & \ddots & \vdots \\ 0 & \cdots & e^{\lambda_i x} \end{pmatrix} C \tag{21}$$

where C is the coefficient matrix associated with the loading conditions.

Let the length of the smallest rod unit in the grid structure model be l. The vibration response from the left endpoint 1 to the right endpoint 2 is described by the transmission matrix equation:

$$S(x_2) = t(l)S(x_1) \tag{22}$$

where $t(l)$ is expressed as follows:

$$t(l) = B_0 \begin{pmatrix} e^{\lambda_1 l} & \cdots & 0 \\ \vdots & \ddots & \vdots \\ 0 & \cdots & e^{\lambda_i l} \end{pmatrix} B_0^{-1} \tag{23}$$

Eq.(22) describes the vibration transmission matrix relationship for a one-dimensional single-beam element. The next step is to extend this formulation to the grid structure. As shown in Fig. 5, the grid structure consists of multiple nodes and interconnected members, with each member unit featuring four input-output points at its ends. This configuration introduces greater complexity compared to a one-dimensional grid structure. For simplification, three degrees of freedom are considered at each point.

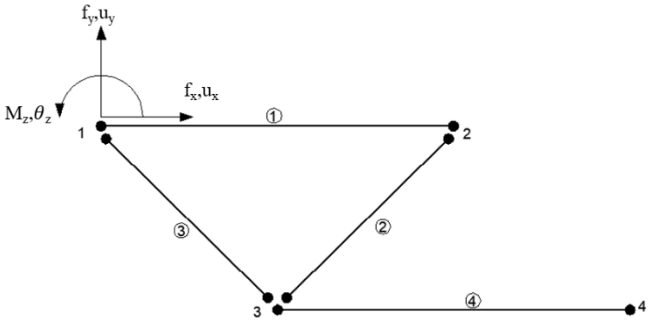

Fig. 5 Vibration analysis model of the smallest unit of grid structure

The relationship between the force and the vibration response is expressed as follows:

$$\{f, g\}_i = \{f_x, f_y, M_z, u_x, u_y, \theta_z\}_i^T \tag{24}$$

where $\{f\}_i$ represents the input force at the i-th interaction point of the selected subunit, and g denotes the vibration velocity response. The vibration response transfer relationship between points i and j at the ends of a rod is expressed in matrix form as follows:

$$\{f, g\}_i = T_{ij}\{f, g\}_j \tag{25}$$

where i and j are from the set (1, 2, 3, 4). The transfer matrix is given as:

$$T_{ij} = \begin{bmatrix} t_{11} & t_{12} \\ t_{21} & t_{22} \end{bmatrix} \tag{26}$$

Using the finite element method, the admittance matrix relationship between points i and j for the grid beam element is obtained as:

$$\{\{g\}_i, \{g\}_j\}^T = H_{ij}\{\{f\}_i, \{f\}_j\}^T \tag{27}$$

In Eq.(27), H is the admittance matrix as follows:

$$H_{ij} = \begin{bmatrix} H_{11} & H_{12} \\ H_{21} & H_{22} \end{bmatrix} \tag{28}$$

In the above equation, H_{11} is the admittance matrix of point i, H_{22} is the admittance matrix of point j, H_{12} and H_{21} are the transfer admittance responses between points i and j. From the admittance matrix equation, the transfer matrix from the input vibration response at point i to the output vibration response at point j is given by:

$$T_{ij} = \begin{bmatrix} -H_{21}^{-1}H_{22} & -H_{21}^{-1} \\ -H_{12}H_{11}H_{21}^{-1}H_{22} & H_{11}H_{21}^{-1} \end{bmatrix} \tag{29}$$

When applied to grid structures, each nodal point within the grid possesses three degrees of freedom, and interactions occur between the degrees of freedom of different connected members. Accordingly, Eq. (26) is modified to become:

$$[T] = \begin{bmatrix} T_{3m\times 3m} & T_{3m\times 3n} \\ T_{3n\times 3m} & T_{3n\times 3n} \end{bmatrix} \tag{30}$$

Since the grid structure is formed by periodic arrangement of the smallest unit cells, the transfer matrix for the grid structure can be derived as:

$$[T] = [T]_1[T]_2[T]_3 \cdots [T]_k \tag{31}$$

According to the theory of elastic dynamics, the elastic wave of simple harmonic vibration can be described by the following equation:

$$\nabla \cdot \big(C(r) : \nabla u(r)\big) + \rho(r)\omega^2 u(r) = 0 \tag{32}$$

Where $\nabla = \left(\partial/\partial x, \partial/\partial y, \partial/\partial z\right)$ is the differential operator, ":" is the double dot product, $u(r)$ is the displacement vector, $r = (x, y, z)$ is the position vector, $\rho(r)$ is the density of the material, and $C(r)$ is the elastic tensor of the material.

In the low-frequency range or near the dominant band gap, the dynamic behavior of the structural unit cell is primarily governed by a finite number of degrees of freedom, represented by its effective mass and equivalent stiffness. Based on the previous derivations, the dynamic transfer matrix of the unit cell is obtained and applied to periodic boundary conditions to derive the dispersion relation. This low-order approximation, rigorously derived from the transfer matrix method, enables accurate prediction of the dynamic characteristics within the primary band gap.

According to Bloch's theorem, the displacement field of a periodic structure can be expressed as:

$$u(r) = e^{i(k\cdot r)}u_k(r) \tag{33}$$

where $i = \sqrt{(-1)}$, $u(r)$ is the displacement field within a unit cell , which shares the same periodicity as the phononic crystal structure. The wave vector $K = (k_x, k_y)$ is constrained to the first Brillouin zone.

When the periodic boundary conditions are applied to the finite element eigenvalue equation for free vibration, it becomes:

$$(K - \omega^2 M)U = 0 \tag{34}$$

This generalized eigenvalue problem with respect to ω^2 is solved by traversing the wave vector k within the irreducible Brillouin zone to obtain the dispersion relationship between the eigenfrequency ω and the wave vector k, thus determining the band gap characteristics of the periodic grid structure.

For the rod- sphere assembly, compared to the sphere, the rod has both relatively smaller mass and stiffness, it can be considered as a unit cell of a phononic crystal, which can be roughly simplified into a spring-mass-spring structure, as illustrated in the Fig. 6.

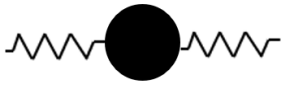

Fig. 6 Spring-mass-spring model

Then, the expression for the starting frequency of the band gap in the simplified model can be given as:

$$f_1 = \frac{1}{2\pi}\sqrt{\frac{k}{M}} \tag{35}$$

where k is the equivalent stiffness of the spring, and M is the equivalent mass.

The derivation of k and M is more complex than that for a two-dimensional phononic crystal unit cell or a metamaterial concrete unit cell. Eq.(35) is intended to reveal the general mechanism and trends of band gap formation rather than to provide precise quantitative predictions.

3. Vibration characteristic of periodic grid rod structures

3.1. Verification of the presence of band gaps in periodic grid rod structures

In order to verify the accuracy of the model in this paper, the calculation results in this paper are compared with the results in the literature[29]. The material parameters and geometric dimensions of the model used in the checking calculation are all from the literature[29]. The model in the text was constructed using COMSOL, as shown in Fig. 7.

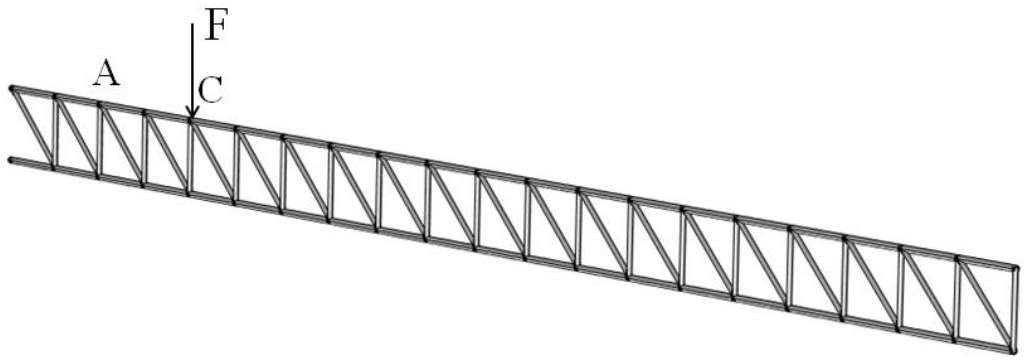

Fig. 7 Truss model in the reference

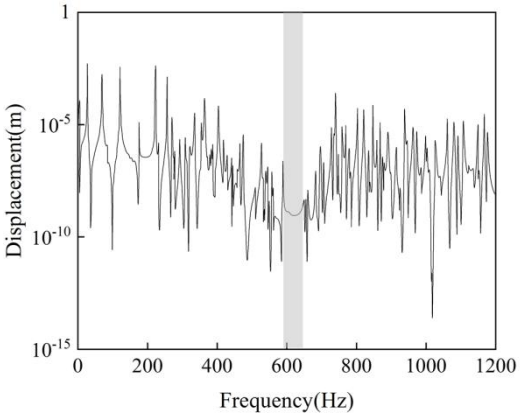

Fig. 8 Frequency-domain calculation results

Fixed constraints are applied at the upper and lower ends on the left side of the structure. A force F of 10 N is applied at point C, and point A is set as the receiving point. The displacement-frequency curve is obtained through frequency-domain analysis, as shown in Fig. 8.

By comparing the stop-band region from the reference literature with the results in Fig. 8, it can be seen that the stop-band obtained from the COMSOL calculation is 585 Hz to 641 Hz, while the reference literature reports a range of 590 Hz to 646 Hz. The value obtained by the finite element calculation is very closed to that found in the literature, so it is thought that the finite calculation is suitable for the calculation of band gap in this paper.

By intentionally altering the material properties of the rods within the grid structure, it is possible to induce distinct band gap characteristics in the system. In this study, a numerical model of the rod elements in a four-sided pyramid grid structure, as illustrated in Fig. 9, was developed using the commercial finite element software COMSOL Multiphysics. In the model, all rods have a uniform length of 4 meters, an outer radius of 0.066 meters, and a wall thickness of 0.006 meters. The spherical nodes possess an outer radius of 0.15 meters and a wall thickness of 0.01 meters.

Fig. 9 Schematic diagram of material grouping of gird rod

As shown in Fig. 9, the single-rod elements of the grid structure are divided into two groups, with the rod on the left named as rod A and the blue rod on the right named as rod B. The material for rod A is selected as steel, while the material for rod B is aluminum. The spherical nodes are all made of steel. The specific material parameters are provided in Table 1.

Table 1
Material parameters of grid rod unit

Material	Density（kg/m^3）	Elastic modulus(GPa)	Poisson's ratio
Steel	7800	200	0.3
Aluminium	2700	70	0.3

From the data in the table 1, it can be observed that the density and Elastic modulus of steel and aluminum differ significantly, resulting in considerable mass and stiffness differences between adjacent rods. This variation facilitates the development of band gap characteristics in the rod elements.

Periodic boundary conditions are applied to both sides of the grid rod elements, restricting displacement along the x-axis. To verify the mesh sensitivity of the rod structure calculations, different mesh sizes were set and analyzed. In this study, a relatively fine mesh was used for the rod calculations, with a maximum element size of 0.44 m and a minimum element size of 0.032 m. For the validation model, an ultra-fine mesh was applied, with a maximum element size of 0.337 m and a minimum element size of 0.0144 m. Both models were then computed separately for comparison. The model is automatically meshed using tetrahedral elements and subjected to a parametric scan for characteristic frequencies, with the first 20 characteristic frequencies obtained. The resulting characteristic frequency graph is shown in Fig. 10.

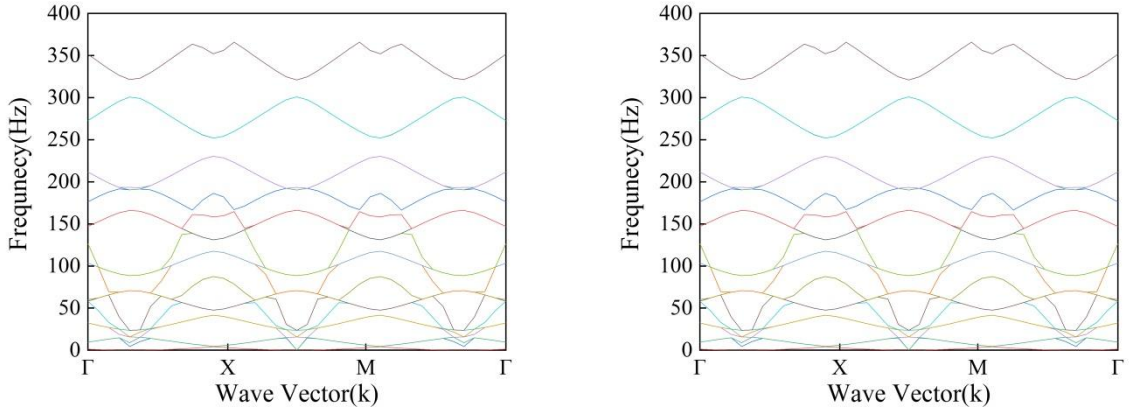

(a) The mesh size is relatively fine (b) The mesh size is ultra-fine

Fig. 10 Grid structure rod unit band gap diagram

As shown in Fig. 10, the calculation results of the model under the two mesh conditions are completely consistent. Therefore, under the mesh conditions used in this study, mesh sensitivity does not affect the model calculations, and the results obtained with this mesh configuration are accurate.

From Fig. 10, it can be observed that the rod structure exhibits two band gaps. The first band gap starts at 230.45 Hz and ends at 252.29 Hz, with a width of 21.84 Hz; the second band gap starts at 300.65 Hz and ends at 321.50 Hz, with a width of 20.85 Hz. This demonstrates that by artificially altering the materials of adjacent rods in the grid structure element, the four-sided pyramid grid structure can achieve its band gap characteristics.

3.2. Analysis of the parameters affecting the band gap of gird structure rod units

According to Eq.(35), the equivalent stiffness influences the value of the band gap. Based on the existing equivalent stiffness calculation equation [42], it is evident that the Elastic modulus of the rods, the cross-sectional dimensions, and the density of the spherical nodes play a crucial role in affecting the starting frequency of the band gap.

To investigate the factors affecting the start frequency, end frequency, and the width of the band gap in grid rod units, an analysis is conducted by varying the material parameters and geometric dimensions to understand their impact on the band gap characteristics of the grid rod units.

3.2.1. Difference in Elastic modulus of adjacent rod materials

Without changing other material parameters and geometric dimensions, only the Elastic modulus of the B rod material is varied. The specific values for the Elastic modulus are provided in Table 2.

Table 2
Elastic modulus of group B

	Elastic modulus（GPa）
Condition 1	0.07
Condition 2	0.7
Condition 3	7
Condition 4	70

The band gap characteristics of the grid rod units under four operating conditions are obtained through calculations, as shown in Fig. 11. The first band gap under different operating conditions is selected for analysis, with its start frequency, end frequency, and width of band gap listed separately for analysis, as shown in Fig. 12.

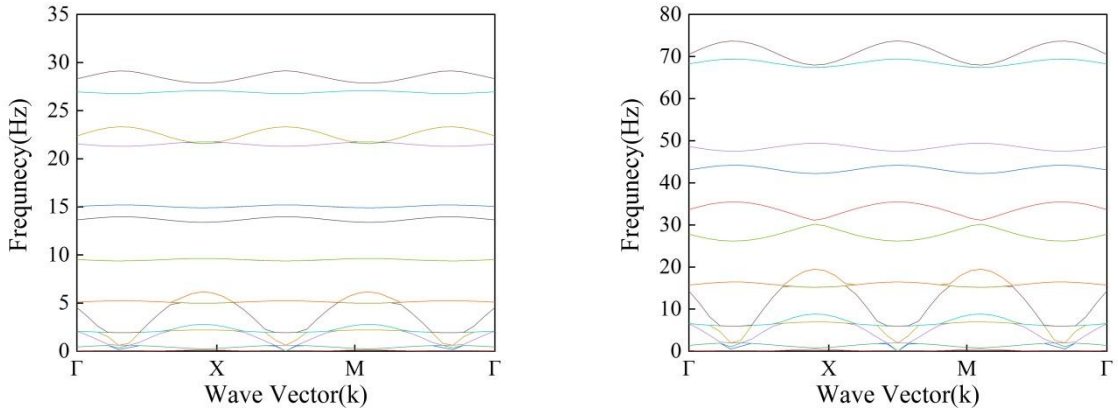

(a) The Elastic modulus of group B is 0.07GPa (b) The Elastic modulus of group B is 0.7GPa

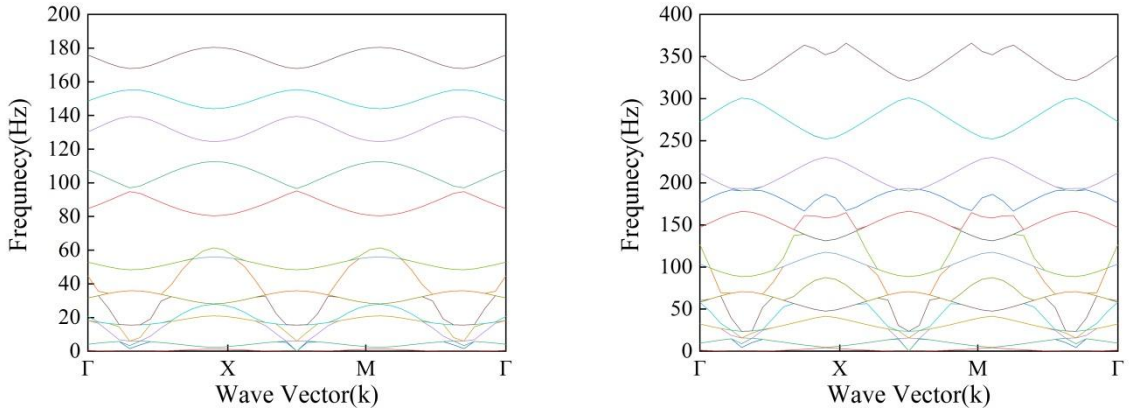

(c) The Elastic modulus of group B is 7GPa (d) The Elastic modulus of group B is 70GPa

Fig. 11 Effect of Elastic modulus of group B on the band gap diagram of grid rod unit

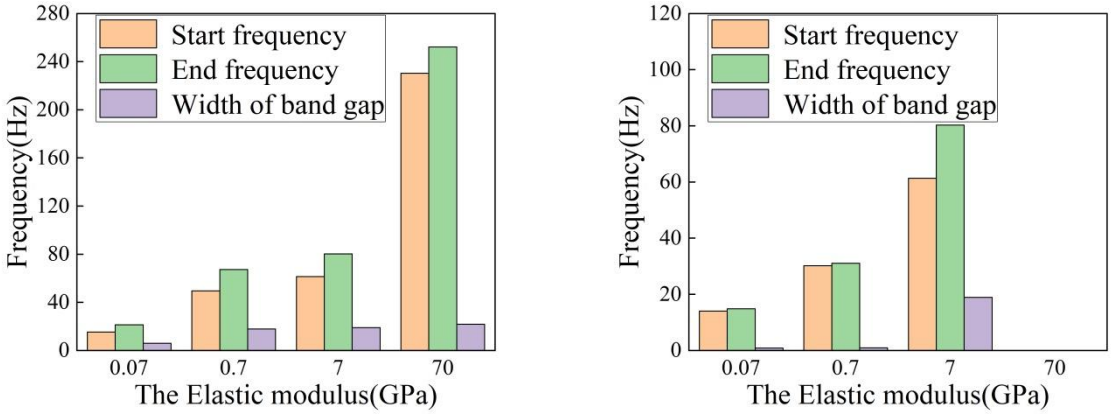

(a) The maximum width band gap (b) The 13th-order band gap

Fig. 12 The variation of band gap diagram under different Elastic modulus conditions for Group B

As shown in Fig. 11 and Fig. 12, when the Elastic modulus of the Group B material is 0.07GPa, four distinct band gaps are observed. The first band gap has a start frequency of 6.16 Hz, an end frequency of 9.40 Hz, and a width of 3.24 Hz. The second band gap starts at 9.73 Hz and ends at 13.36 Hz, with a width of 3.63 Hz. The third band gap, which has the largest width at this modulus, ranges from 15.25 Hz to 21.27 Hz with a width of 6.02 Hz. The fourth band gap spans from 23.34 Hz to 26.71 Hz, with a width of 3.37 Hz. When the Elastic modulus is increased to 0.7GPa, four clear band gaps also appear. The first band gap starts at 19.42 Hz and ends at 26.10 Hz, with a width of 6.68 Hz. The second ranges from 35.56 Hz to 42.11 Hz (width 6.55 Hz), the third from 44.32 Hz to 47.43 Hz (width 3.11 Hz), and the fourth, which has the largest width at this modulus, extends from 49.51 Hz to 66.30 Hz with a width of 17.79 Hz. When the Elastic modulus is 7GPa, four band gaps are again evident. The first band gap, with the largest width at this modulus, ranges from 61.35 Hz to 80.25 Hz, with a width of 18.90 Hz. The second band gap spans 112.79–124.40 Hz (width 11.61 Hz), the third 139.44–144.20 Hz (width 4.76 Hz), and the fourth 155.41–168.02 Hz (width 12.61 Hz). When the Elastic modulus is increased to 70GPa, only two prominent band gaps are observed. The first, which has the largest width across all cases, starts at 230.45 Hz and ends at 252.29 Hz, with a width of 21.84 Hz. The second ranges from 300.96 Hz to 320.98 Hz with a width of 20.02 Hz. If all other material properties and geometric dimensions are held constant, increasing the elastic modulus of Group B raises the natural frequencies of the quadrangular pyramid grid structure. Analysis of the widest band gaps indicates that band gap width generally increases with the elastic modulus of Group B. Given the large number of band gaps present, only one representative band gap is selected for detailed analysis.

By comparing the band gap between the 13th and 14th characteristic frequencies under different conditions of Elastic modulus, it can be observed that when the Elastic modulus of the Group B rods increases, the equivalent stiffness also increases. Consequently, the start frequency, end frequency and the width of band gap for the grid rod unit both increase, however, when the Elastic modulus reaches 70GPa, the 13th-order band gap disappears. This is because as the Elastic modulus of the group B rods increases to 70GPa, the difference in equivalent stiffness between the rods and the spherical nodes decreases, making it difficult for band gaps to form in the low-frequency range. As the natural frequencies of the structure increase, the band gap regions gradually shift toward higher frequencies. For the low-frequency range, when the Elastic modulus of the Group B rods is 7GPa, the value falls within the peak band gap width region; however, for the high-frequency range, 70GPa has not yet reached the peak band gap width region.

3.2.2. Difference in density of adjacent rod materials

Assuming that other material parameters and geometric dimensions remain unchanged, if only the density of the group B material is varied, the specific density values can be found in Table 3.

Table 3
Density values for group B

	Density（kg/m^3）
Condition 1	1000
Condition 2	2700
Condition 3	6000
Condition 4	10000

The band gap characteristics of the quadrangular cone grid structure under four different operating conditions were calculated and are displayed in Fig. 13. The band gap with the largest width under each condition was selected for analysis, with its start frequency, end frequency, and width of band gap presented separately for further examination, as shown in Fig. 14.

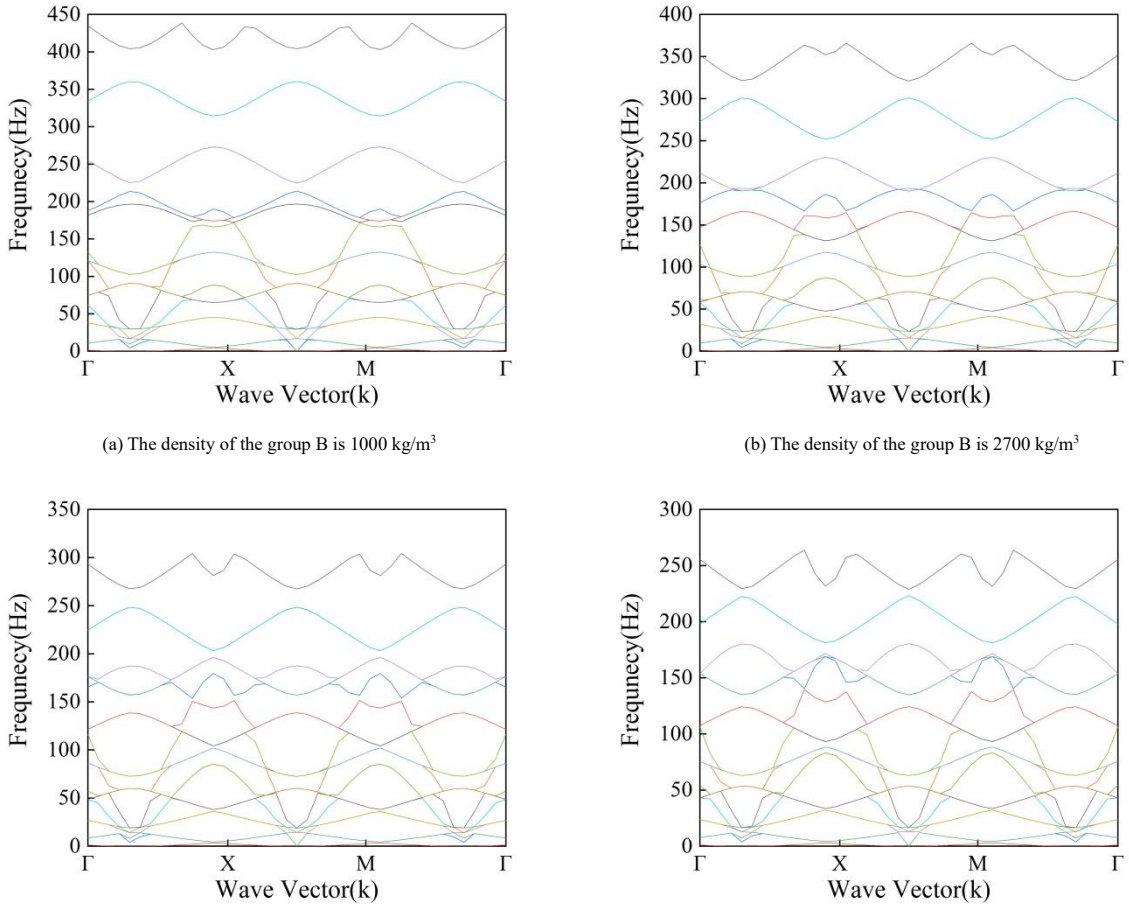

(a) The density of the group B is 1000 kg/m³

(b) The density of the group B is 2700 kg/m³

(c) The density of the group B is 6000 kg/m³

(d) The density of the group B is 10000 kg/m³

Fig. 13 Effect of material density of group B on the band gap diagram of grid rod unit

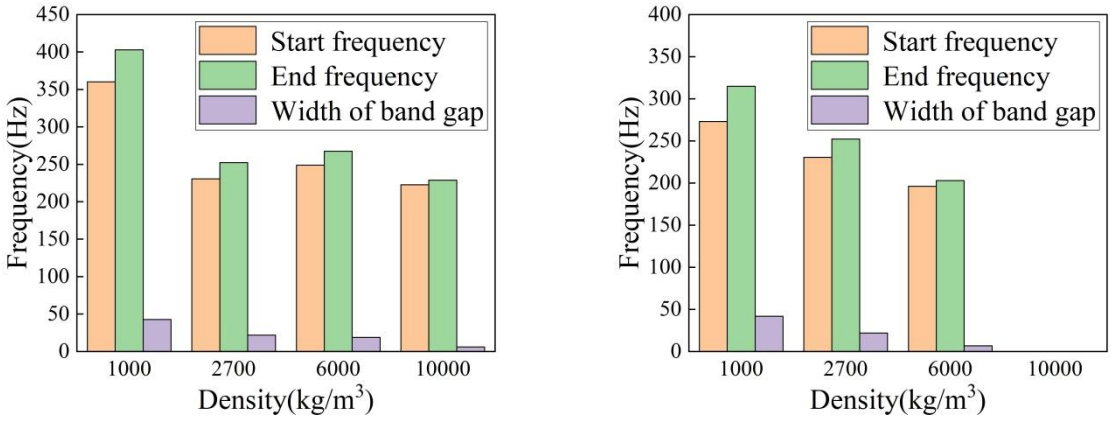

(a) The maximum width band gap

(b) The 16th-order band gap

Fig. 14 The variation of band gap diagram under different density conditions for Group B

As illustrated in Fig. 13 and Fig. 14, when the density of the Group B material is 1000 kg/m³, three distinct band gaps are observed. The first band gap begins at 213.67 Hz and ends at 225.38 Hz, with a width of 11.71 Hz. The second band gap spans from 273.70 Hz to 314.64 Hz, with a width of 40.94 Hz. The third band gap, which has the largest width at this density, extends from 360.10 Hz to 402.89 Hz, with a width of 42.79 Hz. When the density of the Group B material increases to 2700 kg/m³, two clear band gaps emerge. The first band gap, with the largest width, ranges from 230.45 Hz to 252.29 Hz (width 21.84 Hz), and the second spans from 300.96 Hz to 320.98 Hz (width 20.02 Hz). At a density of 6000 kg/m³, two band gaps are also identified. The first starts at 196.10 Hz and ends at 203.81 Hz, with a width of 7.71 Hz. The second, having the larger width, extends from 248.75 Hz to 267.40 Hz, yielding a band gap width of 18.65 Hz. When the density is further increased to 10,000 kg/m³, only a single band gap is present, ranging from 222.75 Hz to 228.86 Hz, with a width of 6.11 Hz. If other material parameters and geometric dimensions remain constant, increasing the density of the Group B material results in a decrease in the self-oscillation frequency of the quadrangular cone grid structure. Moreover, The maximum band gap width initially decreases, then increases, and decreases again with the increase of the density of the Group B rods. This behavior occurs because, as the density of the Group B rods increases, the rate at which the low-frequency band gap width decreases first slows down and then accelerates, while the high-frequency band gap width decrease rate initially accelerates and then slows down. Therefore, at a density of 2700 kg/m³, the low-frequency band gap width surpasses that of the high-frequency band gap region. However, as the density continues to increase, the rate of decrease of the low-frequency band gap width rapidly grows, and the high-frequency band gap width decrease rate diminishes. At a density of 10000 kg/m³, the low-frequency band gap disappears entirely, leaving only the high-frequency band gap present.

By comparing the band gap between the 16th and 17th characteristic

frequencies under different density conditions, it can be observed that as the density of the Group B rods increases, the mass of the rods also increases. Consequently, the start frequency and end frequency of the band gap for the grid rod unit decrease, resulting in a reduction in the width of band gap, until the density reaches 10,000 kg/m³, the 16th-order band gap in the low-frequency range no longer exists. As the density of the rods increases, the density of the Group B rods gradually approaches that of the adjacent rods, reducing the acoustic impedance contrast between neighboring materials. This leads to a decrease in the interface reflection coefficient and an increase in the transmissibility between rods, thereby disrupting the periodic impedance contrast necessary for band gap formation and resulting in the inability to form band gaps.

3.2.3. Difference in inner radius of group B rods

Without changing other material parameters and geometric dimensions, only the density of the Group B material is changed and the specific density values are taken from Table 4.

Table 4
Inner radius of group B

	Inner radius（m）
Condition 1	0.051
Condition 2	0.054
Condition 3	0.057
Condition 4	0.060

The band gap characteristics of the grid rods under four conditions have been calculated and are illustrated in Fig. 15. A band gap with the maximum width under various operating conditions has been selected for analysis, with its start frequency, end frequency, and width of band gap separately listed for examination, as shown in Fig. 16.

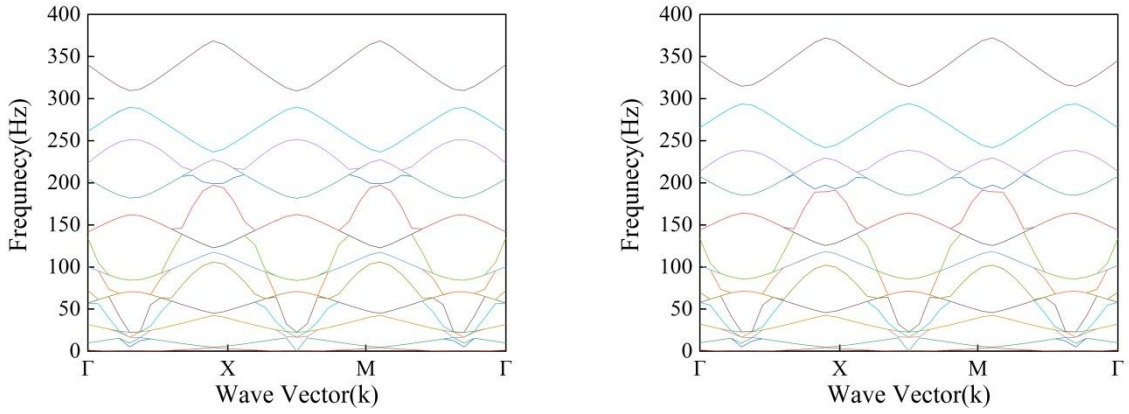

(a) The inner radius of the rod is 0.051 m

(b) The inner radius of the rod is 0.054 m

(c) The inner radius of the rod is 0.057 m

(d) The inner radius of the rod is 0.06 m

Fig. 15 Effect of material density of group B on the band gap diagram of grid rod unit

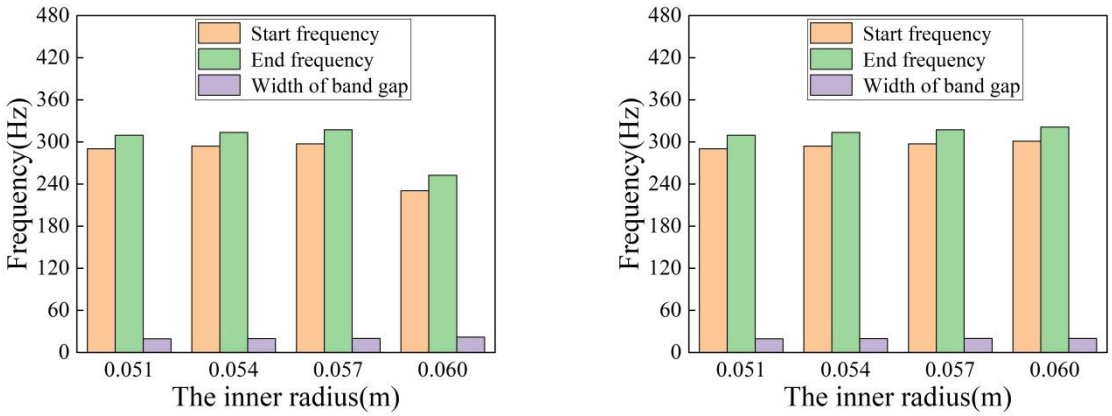

(a) The maximum width band gap

(b) The 19th-order band gap

Fig. 16 The variation of band gap diagram under different inner radius conditions for Group B

As shown in Fig. 15 and Fig. 16, when the inner radius of the Group B rod is 0.051 m, a pronounced band gap is observed, with a start frequency of 290.10 Hz, an end frequency of 309.56 Hz, and a band gap width of 19.46 Hz. When the inner radius is increased to 0.054 m, a similarly clear band gap appears, starting at 294.00 Hz and ending at 313.64 Hz, with a width of 19.64 Hz. When the inner radius reaches 0.057 m, two distinct band gaps are present. The first band gap occurs in the lower frequency range, starting at 231.15 Hz and ending at 246.86 Hz, with a width of 15.71 Hz. The second band gap spans from 297.34 Hz to 317.26 Hz, with a width of 19.92 Hz. When the inner radius is further increased to 0.06 m, two clear band gaps are again observed. The first band gap has the largest width, starting at 230.45 Hz and ending at 252.29 Hz, with a width of 21.84 Hz. The second band gap begins at 300.96 Hz and ends at 320.98 Hz, with a width of 20.02 Hz. If other material parameters and geometric dimensions remain unchanged, by analyzing the largest width of band gap, it can be concluded that the largest width of band gap increases as the inner radius of the Group B rods increases. By comparing the band gap between the 19th and 20th frequencies under different inner radius conditions, it can be seen that as the inner radius increases, both the start frequency, end frequency and width of the band gap increase. As the inner radius gradually increases, high-frequency band gaps gradually decreases. However, the band gap in the low-frequency range appears and gradually widens. This is because as the inner radius of the hollow rods increases, the wall thickness decreases and stiffness reduces. Consequently, the ratio of the bending or longitudinal wave wavelength to the unit cell scale increases, weakening localization effects in the high-frequency range. As a result, high-frequency short waves tend to propagate as nearly continuous waves at the unit cell scale, making it difficult to form high-frequency band gaps.

3.3. Multifactor Analysis

In order to compare the changes in the band gap characteristics of the grid structure rod elements under multiple parameter conditions, the three parameter conditions are calculated for analysis, and the largest width of band gap is selected for further analysis. Table 5 provides a detailed listing of the values for each parameter and their corresponding band gap values.

Table 5
Parameter combinations and their corresponding band gap values

Elastic modulus(GPa)	Inner radius(m)	Density(kg/m^3)	Start frequency(Hz)	End frequency(Hz)	Width of band gap(Hz)
0.07	0.051	1000	23.40	32.00	8.60
	0.051	2700	14.50	20.20	5.70
	0.051	6000	10.20	13.75	3.55
	0.051	10000	8.35	10.78	2.43
	0.054	1000	23.90	32.20	8.30
	0.054	2700	14.75	20.57	5.82
	0.054	6000	10.22	13.95	3.73
	0.054	10000	8.26	10.94	2.68
	0.057	1000	24.20	32.30	8.10
	0.057	2700	15.00	20.90	5.90
	0.057	6000	10.30	14.20	3.90
	0.057	10000	8.20	11.10	2.90
	0.06	1000	24.60	32.40	7.80
	0.06	2700	15.25	21.27	6.02
	0.06	6000	10.43	14.48	4.05
	0.06	10000	8.25	11.25	3.00
0.7	0.051	1000	74.80	94.80	20.00
	0.051	2700	48.83	64.00	15.17
	0.051	6000	37.90	44.28	6.38
	0.051	10000	32.80	35.08	2.28
	0.054	1000	76.00	95.50	19.50
	0.054	2700	49.20	65.12	15.92
	0.054	6000	38.90	44.85	5.95
	0.054	10000	19.04	21.70	2.66
	0.057	1000	77.00	95.70	18.70
	0.057	2700	49.38	66.30	16.92
	0.057	6000	37.62	45.60	7.98
	0.057	10000	18.58	21.92	3.34
	0.06	1000	78.20	96.10	17.90
	0.06	2700	49.51	66.30	17.79
	0.06	6000	36.83	45.60	8.77
	0.06	10000	17.71	21.92	4.21
7	0.051	1000	151.90	185.15	33.25
	0.051	2700	151.50	174.90	23.40
	0.051	6000	117.00	133.27	16.27
	0.051	10000	60.75	66.90	6.15
	0.054	1000	153.80	187.80	34.00

Elastic modulus(GPa)	Inner radius(m)	Density(kg/m^3)	Start frequency(Hz)	End frequency(Hz)	Width of band gap(Hz)
	0.054	2700	153.15	178.10	24.95
	0.054	6000	117.80	135.80	18.00
	0.054	10000	59.90	66.87	6.97
	0.057	1000	108.90	143.46	34.56
	0.057	2700	154.45	181.10	26.65
	0.057	6000	118.00	137.70	19.70
	0.057	10000	58.50	66.83	8.33
	0.06	1000	106.50	146.72	40.22
	0.06	2700	61.35	80.25	18.90
	0.06	6000	68.75	83.50	14.75
	0.06	10000	56.82	66.78	9.96
70	0.051	1000	266.50	304.20	37.70
	0.051	2700	290.10	309.56	19.46
	0.051	6000	241.63	252.80	11.17
	0.051	10000	0.00	0.00	0.00
	0.054	1000	269.00	309.00	40.00
	0.054	2700	294.00	313.64	19.64
	0.054	6000	245.12	257.63	12.51
	0.054	10000	217.50	221.90	4.40
	0.057	1000	271.35	313.17	41.82
	0.057	2700	297.34	317.26	19.92
	0.057	6000	247.50	262.80	15.30
	0.057	10000	220.78	225.50	4.72
	0.06	1000	360.10	402.89	42.79
	0.06	2700	230.45	252.29	21.84
	0.06	6000	248.75	267.40	18.65
	0.06	10000	222.75	228.86	6.11

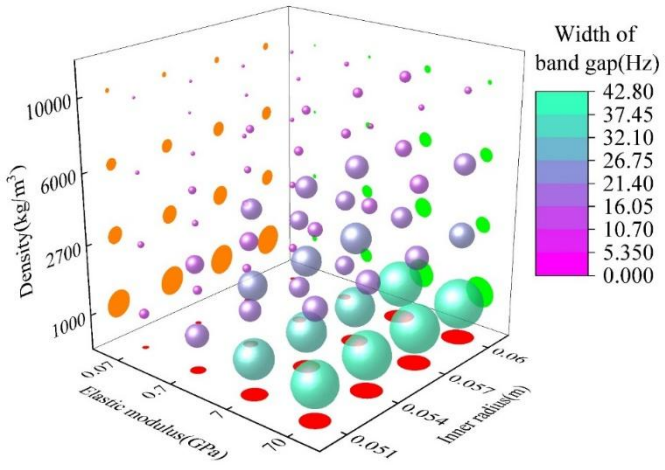

Fig. 17 3D scatter plot of the maximum band gap width under the combined effects of three factors

Based on Table 5 and Fig. 17, for the same density and inner radius conditions, the maximum band gap width increases with the Elastic modulus of the Group B rods. Under high-density and large inner radius conditions, the band gap width is relatively low because the impedance difference between rods decreases, weakening interface scattering effects. A smaller inner radius leads to reduced rod stiffness, which suppresses the formation of high-frequency band gaps. When the Elastic modulus is 0.07GPa or 0.7GPa, for the same Elastic modulus and density, the maximum band gap width decreases as the inner radius of the Group B rods increases. However, when the elastic modulus is 7GPa or 70GPa, under the same Elastic modulus and density, the maximum band gap width increases with increasing inner radius. When both Elastic modulus and density increase simultaneously, the equivalent stiffness difference between rods decreases, and the acoustic impedance contrast reduces, making it difficult to form wide band gaps. For the same Elastic modulus and inner radius, the maximum band gap width decreases as the density of the Group B rods increases. As the rod inner radius increases, wall thickness decreases and stiffness reduces, while the ratio of bending or longitudinal wave wavelength to unit cell scale increases. Additionally, the stiffness difference between adjacent rods diminishes, weakening localization effects in the high-frequency range. Consequently, high-frequency short waves tend to propagate as nearly continuous waves at the unit cell scale, hindering the formation of high-frequency band gaps.

Among the four selected values for each factor, the Elastic modulus undoubtedly has the greatest and most direct influence because it directly affects the equivalent stiffness of the structure. Considering that the Elastic modulus values span orders of magnitude, its impact on band gap values is greater than that of density, which also increases by an order of magnitude. Therefore, the effect of Elastic modulus is more significant than that of density. Compared to the rod inner radius, since the rod volume is proportional to the square of the rod radius, an equivalent numerical change in inner radius has the largest impact on band gap values. However, the range of inner radius variation studied here is very small (on the order of 10^{-3}m), and in practical engineering applications, changing the Elastic modulus through material selection is much easier than drastically altering structural dimensions. Thus, under the conditions studied in this paper, the Elastic modulus has the greatest influence on the structural band gap values, followed by density, with inner radius having the least impact.

4. Attenuation effects of periodic grid structures on shock waves

In order to study the damping effect of the periodic grid structure on vibration loads, the band gap range of the grid structure is determined through simulation calculations. The self-oscillation characteristics and damping effects on shock waves are investigated by applying shocks with different initial frequencies. Specifically, the self-oscillation characteristics of the grid structure and its attenuation effect on the shock wave are examined.

To illustrate the damping effect of the periodic grid structure on the shock wave, the periodic grid structure model shown in Fig. 18 is created by COMSOL Multiphysics software. The model consists of three rod units arranged in a linear direction. To eliminate the influence of boundary effects, a fixed constraint is applied at the rightmost side of the grid structure. An initial excitation is applied to the left side of the model, while a receiver is placed on the right side of the model, as shown in Fig. 18. A total of three conditions are set up for the simulation. In all conditions, the material of the ball nodes is steel. In Condition 1, all rod materials are selected as steel; in Condition 2, all rod materials are selected as aluminium; and in Condition 3, the rod materials are selected according to the material grouping shown in Fig. 9. All material parameters are chosen based on the data provided in Table 1.

A frequency excitation of 240 Hz and 150 Hz was applied separately to the rod structure, with both excitation durations set to 1 second. The chosen excitation frequency of 240 Hz lies within this band gap range (230.45–252.29 Hz), where the structure is expected to suppress the propagation of vibrational waves. In theory, as long as the selected excitation frequency falls within this band gap range, the hybrid rod is expected to provide better attenuation of vibrational wave propagation compared to pure steel and pure aluminum rods. However, in practical engineering and experimental settings, manufacturing tolerances, assembly inaccuracies, and measurement errors can cause discrepancies between the actual band gap range and the simulation results. To facilitate future experimental validation and comparison, it is advisable in simulations to choose an excitation frequency near the midpoint of the band gap range. Therefore, 240 Hz was selected. The expressions are as follows:

$$D_1 = 0.001\,sin(2\pi \times 240t) \tag{36}$$

$$D_2 = 0.001\,sin(2\pi \times 150t) \tag{37}$$

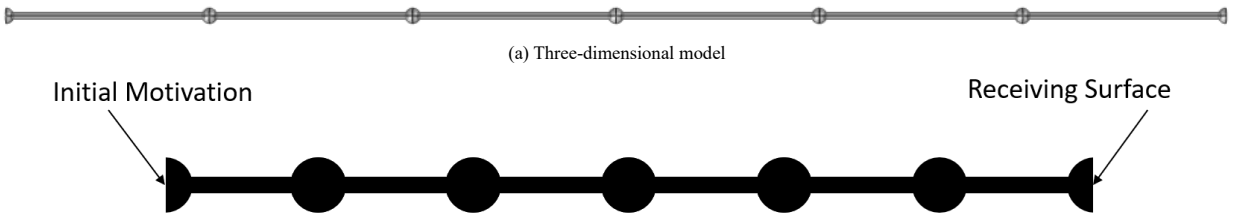

(a) Three-dimensional model

(b) Two-dimensional diagram

Fig. 18 Schematic diagram of grid structure calculation

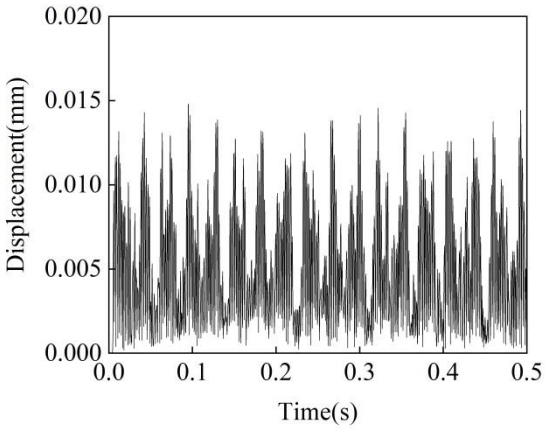

(a)Steel grid structure rods

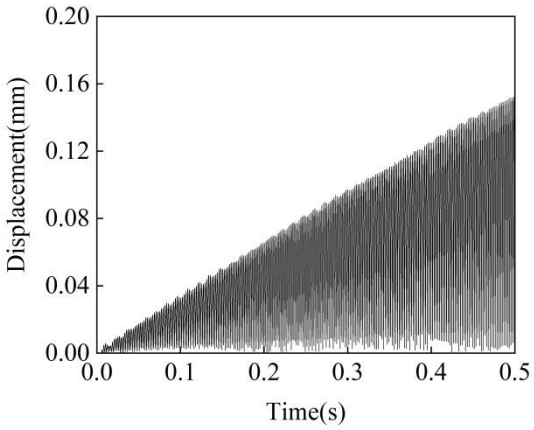

(b)Aluminium grid structure rods

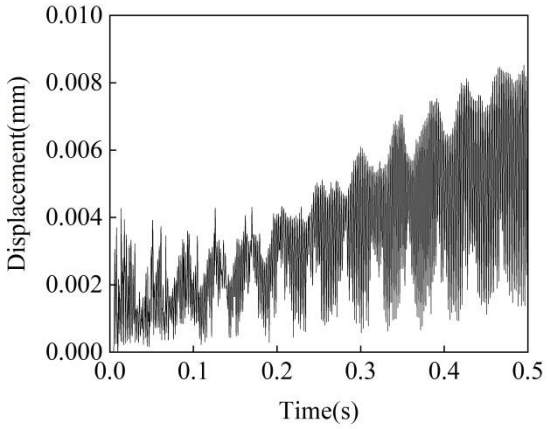

(c)Steel and aluminium hybrid grid structure rods

Fig. 19 Displacement-Time curve of grid rods under D_1

First, the lattice rod structure was subjected to the D_1 excitation, and the displacement time-history curves under different material components were obtained, as shown in Fig. 19. The displacement time histories for the three conditions obtained by transient analysis are shown in Fig. 20. For the steel

grid structure, the peak displacement at the measurement point is 0.0148mm; for the aluminum grid structure, the peak displacement at the measurement point is 0.1526mm; for the steel-aluminum hybrid grid structure, the peak displacement is 0.0085mm. Using the peak displacement of the steel-aluminum hybrid lattice rod as the reference, the peak displacement of the pure steel lattice rod is 174.12% of the reference value, while that of the pure aluminum lattice rod is 1795.29% of the reference value, which proves that the steel-aluminium grid structure rods have better shock wave attenuation than the traditional steel structure grid structure rods.

By applying the Fast Fourier Transform (FFT), the displacement time-history curve in Fig. 19(c) was converted into the displacement frequency-domain curve, yielding displacement responses at different frequencies. Using the Eq.(38), the transmission loss at each frequency was then calculated.

$$\eta = 20lg\left(\mu_{out}/\mu_{in}\right) \tag{38}$$

where μ_{out} refers to the response at the receiving, and μ_{in} refers to the response at the input end.

The calculation results are shown in Fig. 20. As observed from the figure, the transmission curve exhibits significant attenuation within the band gap region of the rod unit, reaching a minimum value of -15.10 dB. This demonstrates that the structure has an effective attenuation capability when subjected to external impacts within the band gap frequency range.

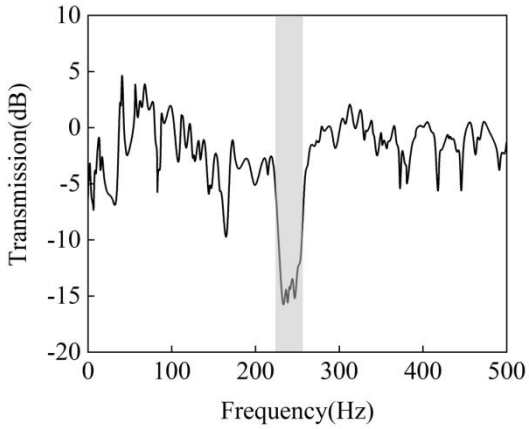

Fig. 20 Transmission loss of the lattice rod structure

For comparison, an D_2 excitation was applied to the lattice rod structure, and the displacement time-history curves for different material components were obtained, as shown in Fig. 21.

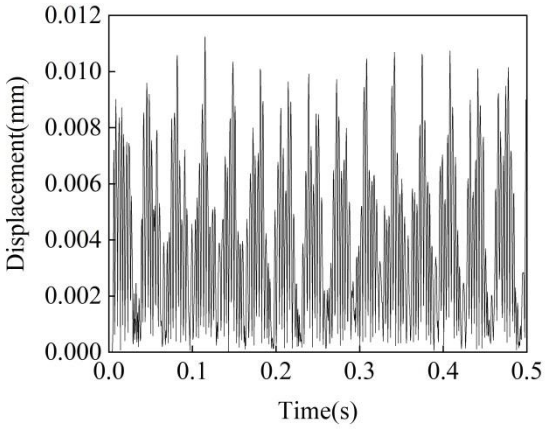

(a) Steel grid structure rods

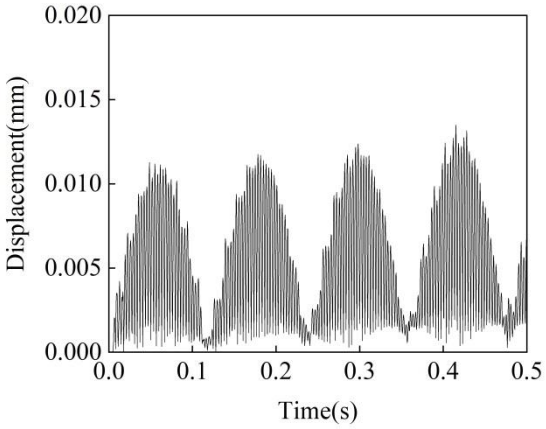

(b) Aluminium grid structure rods

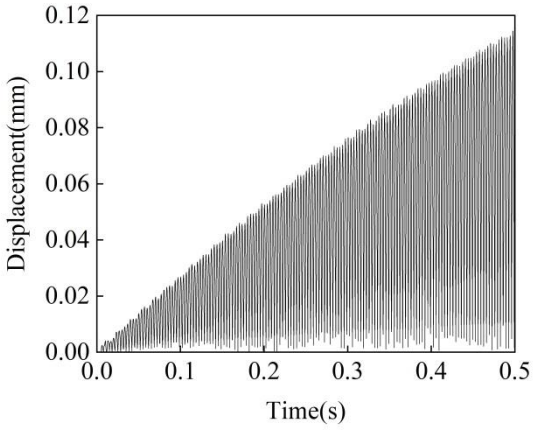

(c) Steel and aluminium hybrid grid structure rods

Fig. 21 Displacement-Time curve of grid rods under D_2

The displacement time histories for the three conditions obtained by transient analysis are shown in Fig. 21. For the steel grid structure, the peak displacement at the measurement point is 0.0112mm; for the aluminum grid structure, the peak displacement at the measurement point is 0.0135mm; for the steel-aluminum hybrid grid structure, the peak displacement is 0.1141mm. Using the peak displacement of the steel-aluminum hybrid lattice rod as the reference, the peak displacement of the pure steel lattice rod is 9.82% of the reference value, and that of the pure aluminum lattice rod is 11.83%. This indicates that when subjected to impacts at frequencies outside the band gap range, the steel-aluminum hybrid rod structure no longer exhibits attenuation. On the contrary, due to its unique material composition, the steel-aluminum hybrid lattice shows poorer attenuation performance against external impacts

compared to the traditional all-steel lattice.

Compared to hybrid rods, steel–aluminum hybrid rods exhibit superior impact wave attenuation not only due to the band gap effect, which filters specific frequency components, but also because the acoustic impedance mismatch at material interfaces leads to multiple wave scatterings and partial reflections. In an ideal periodic structure, conceived as an infinite repetition of unit cells, the cumulative effect of interface scattering gives rise to the formation of band gaps. However, in practical scenarios, the size of a periodic structure is finite. The actual attenuation effect arises from the combined action of energy suppression within the band gap frequency range and multiple interface scatterings outside the band gap range. The band gap effect and wave scattering are interrelated and jointly operative mechanisms: interface scattering is the physical basis for band gap formation, while in finite structures it also independently contributes to broadband impact energy dissipation.

Although steel–aluminum hybrid rods can effectively suppress impact waves and vibrations through band gap effects and impedance scattering, several challenges exist in practical engineering applications. First, due to the significant difference in thermal expansion coefficients between steel and aluminum, the interface is prone to residual stresses and potential cracking under thermal cycling, requiring specialized joining techniques to ensure interface integrity. Second, the formation of galvanic couples between the two metals can lead to electrochemical corrosion in humid or saline environments, necessitating effective isolation coatings or cathodic protection measures, which increase manufacturing and maintenance costs. Additionally, achieving standardized and modular structural designs is more complex.

In order to further understand the attenuation mechanism, A frequency sweep analysis was conducted on the structure shown in Fig. 18 under the following conditions: an initial prescribed displacement of 10^{-6} m was applied to the leftmost end of the structure, a receiving surface was positioned at the rightmost end, and low-reflection boundary conditions were imposed on both the left and right ends. The frequency sweep spanned from 10Hz to 300Hz with a 1Hz interval. In Condition 1, all rod materials are selected as steel; in Condition 2, all rod materials are selected as aluminium; and in Condition 3, the rod materials are selected according to the material grouping shown in Fig. 9. All material parameters are chosen based on the data provided in Table 1.

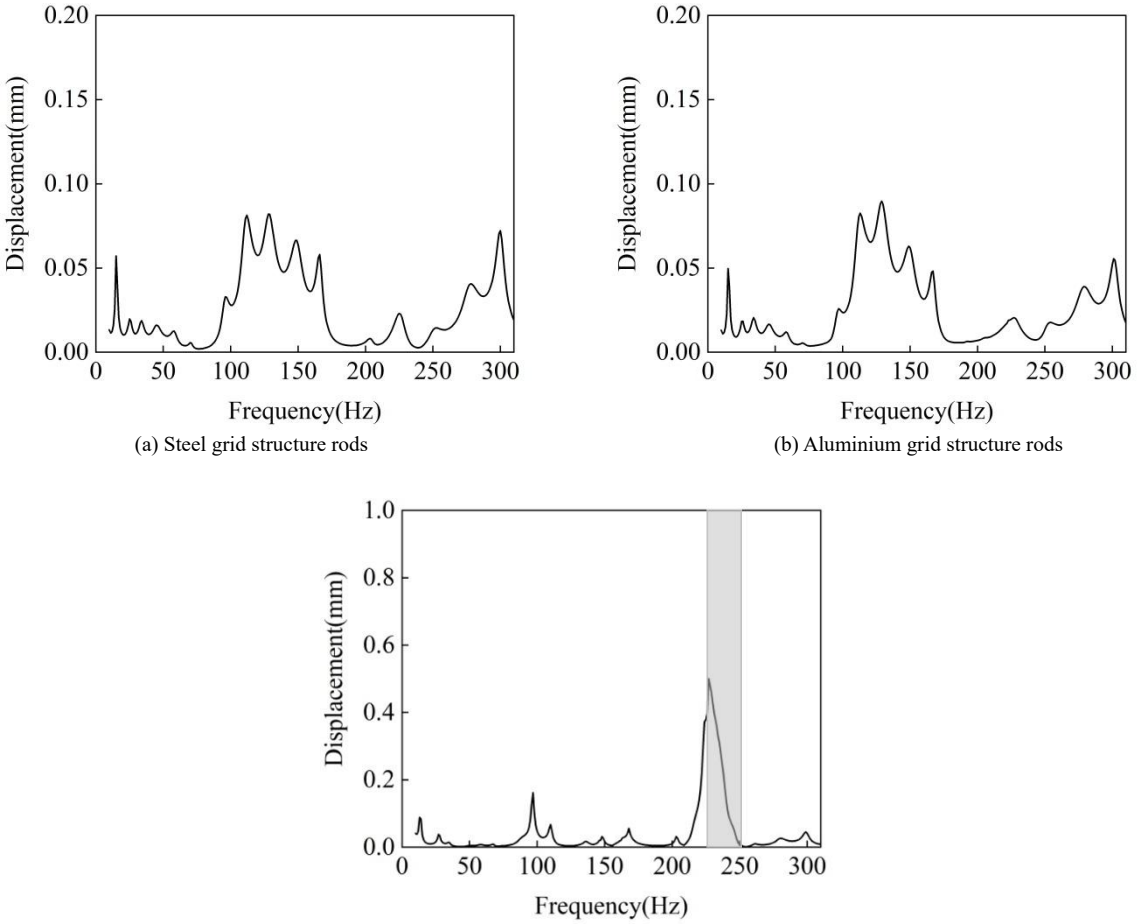

(a) Steel grid structure rods

(b) Aluminium grid structure rods

(c) Steel and aluminium hybrid grid structure rods

Fig. 22 Frequency-Displacement curve of grid rods

Fig. 22 shows that for the steel grid and aluminum grid structures, the displacement at the measurement point exhibits no significant attenuation across the 10Hz–300Hz frequency range. However, for the steel-aluminum hybrid grid structure, a prescribed displacement attenuation is observed within the frequency range of 225.53Hz to 253.74Hz, where the displacement decreases from 0.56mm to 0.003mm. As shown in Fig. 9, the band gap of the steel-aluminum hybrid single-bar structure spans 230.45Hz to 252.29Hz, which lies entirely within the displacement attenuation frequency range. This confirms that the steel-aluminum hybrid grid structure exhibits significant attenuation for waves within the band gap frequency range. Furthermore, this result demonstrates that the band gap characteristics of the single-bar structure play a critical role in suppressing vibrations across the entire grid structure.

5. Conclusion

In order to study the vibration reduction and isolation effects of periodic grid structures, this paper analyzes the band gap characteristics of the grid rod units and their shock wave attenuation effects, and draws the following conclusions:

(1) The grid structure is a typical periodic structure, and the analysis methods for periodic structures can be applied to the grid structure. The grid rod unit can be roughly simplified into a spring-mass spring mechanical model, and its band gap calculation equation can reflect the variation of parameters. By intentionally modifying the grid structure, its band gap characteristics can be achieved.

(2) Rods with low Elastic modulus can form low-frequency band gaps, but the width of band gap is narrow, with the increase of the Elastic modulus of the group B, the start frequency, end frequency, and width of the 13th-order band gap and the largest width band gap all increase, however, when the Elastic modulus reaches 70GPa, the 13th-order band gap disappears, meaning the low-frequency band gap vanishes, while the high-frequency band gap width continues to increase. Rods with lower density can form wider band gaps, with

the increase of the density of the group B, the largest width of band gap gradually decreases, The starting frequency, end frequency, and bandwidth of the 16th-order band gap all decrease, and the 16th-order band gap disappears when the density reaches 10,000 kg/m³. As the inner radius of the group B increases, the starting frequency, end frequency, and bandwidth of the 19th-order band gap all increase. When the inner radius of the group B reaches 0.057 m, a low-frequency band gap appears, and its bandwidth continues to increase with the inner radius.

(3) Compared to steel grid structure rods and aluminium grid structure rods, the steel-aluminium hybrid grid structure rods exhibit stronger attenuation effects on shock waves, the band gap characteristics of the single-bar structure play a critical role in suppressing vibrations across the entire grid structure.

(4) Compared to traditional dampers, the hybrid rod solution offers inherent broadband vibration suppression potential within the structure itself, without relying on external power or maintenance, providing better life cycle cost advantages in enclosed and temperature controlled environments. However, under conditions of high corrosion or significant temperature variations, conventional viscous or friction dampers, due to their mature manufacturing processes, simple maintenance, and flexible design, may be more competitive in terms of cost and reliability. Therefore, the design and application of steel and aluminum hybrid rods require a comprehensive life cycle cost benefit analysis tailored to specific operating conditions.

Acknowledgement

This research was funded by National Natural Science Foundation of China, grant number (12172244).

Declaration

The authors declare that they have no known competing financial interests or personal relationships that could have appeared to influence the work reported in this paper.

Appendix

S_1: State vector at endpoint 1;
S_2: State vector at endpoint 2;
f: the external load of the rod;
M: the torque;
u: the displacement value of the vibration response;
θ: the angular displacement value of the torsional response;
ρ: the material density;
h: the equivalent height of beam section;
R_m: the bending beam radius of curvature;
G: the shear stiffness;
κ: the shear constant;
ω: angular frequency;
C: the coefficient matrix associated with the loading conditions;
$\{f\}_i$: the input force at the i-th interaction point of the selected subunit;
g: the vibration velocity response;
H: the admittance matrix;
∇: the differential operator;
$u(r)$: the displacement vector;
$r = (x, y, z)$: the position vector;
$\rho(r)$: the density of the material;
$C(r)$: the elastic tensor of the material;
$u_1(r)$: the displacement field within a unit cell;
K: the wave vector;
k: the equivalent stiffness of the spring;
M_1: the equivalent mass;
μ_{in}: input response;
μ_{out}: output response.

Reference

[1] Li H W. Planning and Design of Urban Disaster Earthquake Shelters and Disaster Relief Strongholds[M]. China Architecture and Building Press, 2013.
[2] Ding B D, Lv H L, Li X, et al. Tests for dynamical progressive collapse of a grid structure based on key member failure[J]. Journal of Vibration and Shock. 2015, 34(23):106-114.
[3] Adam J M, Parisi F, Sagaseta J, et al. Research and practice on progressive collapse and robustness of building structures in the 21st century[J]. Engineering Structures, 2018, 173(OCT.15):122-149.
[4] Xue H, Wang H, Liu X G. Effects of supporting-substructure lateral stiffness on the internal forces of grid structures[J]. Journal of Constructional Steel Research, 2025, volume 224, part A, 109155.
[5] Lord rayleigh, On the maintenance of vibrations by forces of double frequency and on the propagation of waves through a medium endowed with a periodic structure, Philosophical Magazine XXIV, 1887, 145-159.
[6] Floquet G. Sur les équations différentielles linéaires à coefficients périodiques[J]. Annales Scientifiques de l'Éolecole Normale Supérieure, 1883, 12: 47-88.
[7] Bloch F. Über die quantenmechanik der electronen in kristallgittern[J]. Zeitschrift Für Physik AHadrons & Nuclei, 1929, 52:555-600.
[8] Mead D M. Wave propagation in continuous periodic structures: research contributions from Southampton[J]. Journal of Sound and Vibration, 1996, 190(3):495-524.
[9] Zhu X, Li T Y, Zhao Y. Vibration energy flow characteristics and damage identification of crack damaged structures[M], Huazhong University of Science and Technology Press, 2017.
[10] Zhao X Z, Yan S, Chen Y Y. Comparison of progressive collapse resistance of single-layer latticed domes under different loadings[J]. Journal of Constructional Steel Research, 2017, 129(Complete):204-214.
[11] Sigalas M M, Economou E N. Elastic and Acoustic wave band structure[J]. Journal of Sound and Vibration, 1992, 158(2):377-382.
[12] Wang D Z, Zhi X D, Fan F, et al. The energy-based failure mechanism of reticulated domes subjected to impact[J]. Thin Walled Structures, 2017, 119:356-370.
[13] Lin L. Refined study on impact response and failure of reticulated shells[D]. Harbin Institute of Technology, 2015.
[14] Brun M, Movchan A B, Jones I S. Phononic band gap systems in structural mechanics: finite slender elastic structures and infinite periodic waveguides [J].Journal of Vibration and Acoustics, 2013, 135(4):041013.1-041013.9.6.
[15] Gao M, Kong X L, Zhao L Z, et al. Study on band gap characteristics of periodic structural wave impeding block[J]. China Civil Engineering Journal, 2022:11.
[16] Xiong Y H, Li F M. Optimization of Band-gap Characteristics of Hierarchical Periodic Beam[J]. Chinese Journal of Solid Mechanics, 2021, 42 (06)：634-641.
[17] MUHAMMAD, LIM C W, YAW Z, et al. Periodic and a-periodic 3-D composite metastructures with ultrawideband gap for vibration and noise control[J]. Composite structures, 2022, 287: 115324.
[18] Liu Y, An X Y, Chen H L, et al. Vibration attenuation of finite-size meta-concrete: Mechanism, prediction and verification[J]. Composites Part A: Applied Science and Manufacturing, 2021, Volume 143,106294.
[19] Zhang E, Lu G Y, Yang H W et al. Band gap characteristics of metamaterial concrete and its attenuation effect on shock wave[J]. Explosion and Shock. 2020,40(6):66-74.
[20] Han J, Lu G Y. A study of undamped free vibration characteristics on a metaconcrete unit cell[J]. Vibration and Shock, 2021, 40(08), 173-178+215.
[21] Xu C, Chen W S, Hao H. The influence of design parameters of engineered aggregate in metaconcrete on band gap region[J]. Journal of the Mechanics and Physics of Solids, 2020, 139:103929.
[22] Akintoye O. Oyelade *, Yetunde. O. Abiodun , Mufutau O. Sadiq. Dynamic behaviour of concrete containing aggregate resonant frequency[J]. JCAMECH, 2018.269048.339.
[23] Feng L, Liu X P, Lu M H, et al. Refraction control of acoustic waves in a square-rod constructed tunable sonic crystal[J]. Physical Review B, 2006, 73(19):193101.
[24] Shen H J. Control of Sound and Vibration for Seawater Pipe System Based on Phononic Ctrystal Theory [D]. National University of Defense Technology, 2015.
[25] Zhao X Z, Yan S. Mechanisms of Continuous Collapse of Space Structures and Design Countermeasures[M]. China Architecture and Building Press, 2018.
[26] Wen X S, Wen J H, Yu D L, et al. Phononic Crystals[M]. National Defense Industry Press, 2008.
[27] Wen J H, Yu D L, Zhao H G, et al. Elastic wave propagation in artificial periodic structures: vibrational and acoustic properties [M]. China Science Publishing & media Ltd., 2016.
[28] An X Y, Lai C L, He W P, et al. Three-dimensional meta-truss lattice composite structures with vibration isolation performance[J]. Extreme Mechanics Letters, 2019, 33.
[29] ZUO S L, LI F M, ZHANG C Z. Numerical and experimental investigations on the vibration band-gap properties of periodic rigid frame structures[J]. Acta mechanica, 2016, 227(6): 1653-1669.
[30] Meruane V, Puiggros I, Fernandez R, et al. Efficient design of sandwich panels with cellular truss cores and large phononic band gaps using surrogate modeling and global optimization[J]. Frontiers in Mechanical Engineering, 2024, volume 10.
[31] Quinteros L, Meruane V, Cardoso E L. Phononic band gap optimization in truss-like cellular structures using smooth P-norm approximations[J]. Structural and Multidisciplinary Optimization, 2021, volume 64, pages 113-124.
[32] Brun M, Movchan A B, Jones I S. Phononic band gap systems in structural mechanics: finite slender elastic structures and infinite periodic waveguides[J]. Journal of Vibration and Acoustics, 2013, 135(4):041013.1-041013.9.
[33] Michele B, Felice G G, Movchan A B, et al. Transition Wave in the Collapse of the San Saba Bridge[J]. Frontiers in Materials, 2014, 1.
[34] Meng Q J, Shi Z F. Ambient vibration attenuation by periodic pile barriers using periodic theory and COMSOL PDE method [J]. Rock and Soil Mechanics, 2018, 39(11):343-352.
[35] Cherepanov G P. Mechanics of the WTC collapse[J]. International Journal of Fracture, 2006, 141(1-2):287-289.
[36] Dal Poggetto V F, Serpa A L. Flexural wave band gaps in a ternary periodic metamaterial plate using the plane wave expansion method[J]. Journal of Sound and Vibration, 2021, 495.
[37] V. F D P, Alberto L S. Elastic wave band gaps in a three-dimensional periodic metamaterial using the plane wave expansion method[J]. International Journal of Mechanical Sciences, 2020, 184.
[38] Hong X, Guo W J, Dai C X. Effect of Hysteresis Damping on Vertical Vibration Band Gap Characteristics of Periodic Track Structure[J]. Journal of East China Jiaotong University, 2023, 40(01):82-91.
[39] S. K A. Multichannel tunable polarizing filter properties of one-dimensional ternary photonic crystal containing single-negative materials[J]. Indian Journal of Physics, 2021: 1-11.
[40] Shahsavari H, Talebitooti R, Kornokar M. Analysis of wave propagation through functionally graded porous cylindrical structures considering the transfer matrix method[J]. Thin-Walled Structures, 2021, 159.
[41] Threetanya P, Puttharaksa C, Plaipichit S, et al. Recursive transfer-matrix method for second-harmonic generation in a one-dimensional nonlinear photonic crystal at arbitrary incidence angle[J]. Journal of Physics: Conference Series, 2021, 1719(1).
[42] Zhao H X, Zhang E, Lu G Y. Study on the equivalent stiffness of a local resonance metamaterial concrete unit cell[J]. Buildings, 2024, (14):1035.